Evaporation Model for Keyhole Dynamics During Additive Manufacturing of Metal

Lu Wang,[1] Yanming Zhang,[2] and Wentao Yan[1,*]

[1] *Department of Mechanical Engineering, National University of Singapore, 117575, Singapore*
[2] *Department of Mechanical Engineering, Tsinghua University, Beijing 100084, China*

(Received 4 July 2020; accepted 27 October 2020; published 14 December 2020)

The molten-pool flow, particularly the keyhole effect, plays a critical role in the formation of defects in additive-manufacturing and welding processes. In this study, we derive an evaporation model for metal alloys considering the gas-flow structure and material composition and implement it in a multiphysics thermal-fluid flow model, which utilizes the volume of fluid (VOF) in the finite volume method (FVM) to capture free surfaces and the ray-tracing method to track multireflections of laser within the keyhole. The current derived evaporation model is validated against *in situ* x-ray imaging results via multiple cases: (1) stationary laser melting of a Ti-6Al-4V base plate under 1-atm ambient pressure, (2) stationary laser melting of a 304L stainless-steel base plate under 0.0002-atm ambient pressure, (3) laser scanning of a Ti-6Al-4V base plate under 1-atm ambient pressure. The simulation results indicate that our evaporation model is applicable for both common and near-vacuum environment, while Anisimov's evaporation model, which is widely used in keyhole simulation, is unsuitable in near-vacuum keyhole simulation. Moreover, the absorbed energy distribution, recoil pressure, z-direction recoil force and keyhole growth are analyzed in the simulations.

DOI: 10.1103/PhysRevApplied.14.064039

I. INTRODUCTION

Additive manufacturing (AM) has gained increasing attention over the past several decades, for its ability to fabricate products with complex geometry [1], and manufacturing functionally graded materials [2]. Selective laser melting (SLM), direct energy deposition (DED), and electron beam melting (EBM), are promising approaches to manufacture products with fascinating characteristics, such as lighter weight and better mechanical properties. However, the defects, such as pores and cracks, degrade the quality of as-built parts and hinder the applications in various industries. There are some possible reasons, e.g., the lack of fusion and the keyhole phenomenon for these defects. To better understand the source of porosity, this paper focuses on the keyhole phenomenon [3–5].

To observe the keyhole formation, optical imaging is adopted in the laser-welding process [6,7]. These investigations, in most cases, can only provide surface geometry from the top and side views or plume above the molten-pool surface. When it comes to the laser powder-bed-melting process, the smaller molten-pool size and severe keyhole fluctuation dramatically increase the observation difficulty. Therefore, optical imaging is mainly applied to observe keyhole-induced plume [8,9] and powder-bed denudation [10] in the AM process. To observe keyhole dynamics directly, researchers turn to the x-ray imaging method [11–15], which provides more accurate data of the keyhole through *in situ* observation without disturbing the melting process. Recently, Allen *et al.* [16] explored the positive correlation between the keyhole geometry and laser energy absorptance with real-time measurement techniques and confirmed it with a ray-tracing predictive model. These investigations have collected data to explain the relation between manufacturing parameters (e.g., laser power and scanning speed) and keyhole geometry features.

However, these experimental results are far from sufficient to reveal the detailed keyhole mechanisms. Numerical simulation offers a promising approach to investigate the molten-pool flow. Recently, some multiphysics thermal-fluid models [17–21] based on the finite volume method (FVM) and lattice Boltzmann method (LBM) have been developed to investigate the molten-pool evolution, where the level-set (LS), volume of fluid (VOF), and arbitrary Lagrangian-Eulerian (ALE) methods are adopted to track the free surface.

To simulate the keyhole dynamics, the recoil pressure, mass loss, and heat loss in the evaporation process are critical. The gas kinetic theory was first implemented by Hertz [22] to study the evaporation in vacuum. In 1953, Schrage and Kucherov [23] proposed a corrected Hertz-Knudsen function from Knudesen and Risch's theory [24,25] by

*mpeyanw@nus.edu.sg

 © 2020 American Physical Society

taking the vapor bulk-velocity effect into consideration. Knight [26] extended the evaporation model from vacuum environment to the common environment for a pure material. Anisimov [27] and Yrehus [28] modified previous models and built up full dynamics relations for both sides of the Knudsen layer.

By incorporating the previous evaporation model into the multiphysics thermal-fluid models, the study of keyhole phenomenon [29,30] has reached some progress. Kouraytem *et al.* [31] investigated the energy distribution and driving forces on the wall of the keyhole surface in the molten-pool-dynamics simulations. Bayat *et al.* [32] simulated the keyhole-induced porosities in laser powder-bed fusion considering the recoil pressure caused by evaporation. Khairallah *et al.* [19] implemented an evaporation model to study the formation mechanisms of pores, spatter, and denudation during the melting process.

For the aforementioned keyhole-dynamics simulation cases, the evaporation mass and recoil pressure were calculated via Anisimov's model [27], which did not fully consider the ambient gas-flow structure and metal compositions. In this study, an evaporation model incorporating these effects is derived from thermodynamics and integrated with the multiphysics thermal-fluid model to simulate molten-pool fluid dynamics. The multiphysics thermal-fluid model utilizes the VOF method [33] to capture the free surface and the ray-tracing method [34] to track the laser-reflection process.

In Sec. II, we derive the mass, momentum, and energy-flux functions in a steady evaporation process and describe the multiphysics thermal-fluid flow model. In Sec. III, the current evaporation model is compared with Anisimov's evaporation model under different ambient pressure with different alloys; further, the stationary laser keyhole on a base plate with different materials are simulated in common and near-vacuum environment and validated against the x-ray imaging results, as well as compared with Anisimov's evaporation model; finally, laser-scanning keyhole simulations are validated against the experimental images, where the recoil pressure, recoil force, and energy distribution on the wall of the keyhole with different laser-scanning speeds are further analyzed.

II. METHODOLOGY

A. Evaporation model

1. Flow field of the Knudsen layer

According to the previous evaporation models [23,26–28], the flow structure mainly consists of the transition layer, Knudsen layer, and vapor phase above the liquid surface, as shown in Fig. 1. A transient layer exists near the condensed phase surface where matter density changes monotonically from liquid state to gas state rapidly [35]. The thickness of transition layer is extremely small (about a few molecule diameters) and it can be simplified as discontinuity. The Knudsen layer is a kinetic boundary layer between the transient layer and external continuum vapor flow, where the vapor is in nonequilibrium state. The thickness of Knudsen layer is in the same order of magnitude as the mean free path of gas molecules.

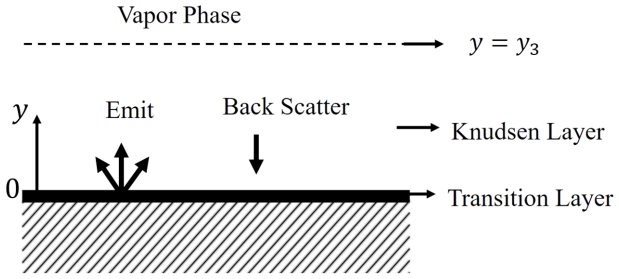

FIG. 1. Schematic of the Knudsen layer. The origin is on the top surface of the transition layer and y positive direction is the evaporating direction. $y = y_3$ is the interface between vapor phase and Knudsen layer.

The continuum theory cannot be applied in the Knudsen layer, because statistical averaging loses their macroscopic sense at the nonequilibrium state [28]. Generally, the Boltzmann equation gives an appropriate description of transport phenomena at the scale of the molecular mean free path. The evaporating molecules on the liquid surface could be divided into two parts: the emitting molecules and back-scatter molecules as shown in Fig. 1. Based on Hertz's study [22], the distribution function of emitting molecules follows the Maxwell distribution. A fraction of back-scatter molecules condense on the liquid surface, and others are reflected in either diffusive or specular reflection pattern. For condensation on the liquid surface, the back-scatter molecules might collide with one or more molecules in the liquid due to the loose packing of molecules in the liquid phase [36]. That means, the back-scatter molecules could exchange energy and momentum sufficiently with the liquid phase. Williams [37] proved that nearly all the back-scatter molecules would condense on the surface for metals with monatomic vapor.

On the evaporating surface ($y = 0$), the velocity distribution of the emitting and condensing molecules are

$$f(\vec{x},\vec{\xi},t) = \begin{cases} \dfrac{n_e}{(2\pi RT_e)^{3/2}} \exp^{-\vec{\xi}^2/2RT_e} & \xi_y > 0 \\ \dfrac{\beta n_3}{(2\pi RT_3)^{3/2}} \exp^{-(\vec{\xi}-\vec{u})^2/2RT_3} & \xi_y \le 0, \end{cases} \tag{1}$$

where f is the velocity distribution function of vapor molecules, and $\vec{x}$, $\vec{\xi}$, and t are position, velocity, and time, respectively. $n_e = \rho_e/m_e$ is the number density of emitting molecules. ρ_e and m_e are the saturated vapor density and molecule mass on the liquid surface with the temperature T_e. $n_3 = \rho_3/m_e$, ρ_3, and T_3 are the number density,

mass density, and temperature of vapor at $y = y_3$. $R = k_B/m_e$ is the specific gas constant of vapor, where k_B is the Boltzmann constant 1.3806×10^{-23} m^2 kg/(s^2 K). $\vec{u} = (0, u_3, 0)$ is the bulk velocity of the vapor. $\xi_y > 0$ and $\xi_y \leq 0$ refer to the emitting and condensing molecules' velocity at $y = 0$, respectively. We ignore the recession velocity of the liquid surface since it is quite small compared with the bulk velocity of vapor, less than 1% of the vapor bulk velocity. β is the condensation ratio, which is given later.

The velocity distribution function on $y = y_3$ is assumed to be local equilibrium (local Maxwell distribution):

$$f(\vec{x}, \vec{\xi}, t) = \frac{n_3}{(2\pi RT_3)^{3/2}} \exp^{-(\vec{\xi}-\vec{u})^2/2RT_3}. \tag{2}$$

For the steady evaporation, the Boltzmann equation is

$$\xi_y \frac{\partial f}{\partial y} = Q(f, f_*), \tag{3}$$

where $Q(f, f_*)$ is the two-body collision integration between gas molecules [36]. Integrating Eq. (3) with variable $\psi_i = m_e,\ m_e\xi_y,\ m_e\xi^2$ $(i = 1, 2, 3)$ in whole velocity space Γ^3 represents mass, momentum, and kinetic-energy-conservation equations. The integration turns to be zero on the right side due to the elastic collision assumption in the Boltzmann equation.

$$\frac{\partial}{\partial y} \int_{\vec{\xi}\in\Gamma^3} \psi_i \xi_y f d\vec{\xi} = \int_{\vec{\xi}\in\Gamma^3} \psi_i Q(f, f_*)\, d\vec{\xi} = 0. \tag{4}$$

That is,

$$\left(\int_{\vec{\xi}\in\Gamma^3} \psi_i \xi_y f d\vec{\xi}\right)_{y=0} = \left(\int_{\vec{\xi}\in\Gamma^3} \psi_i \xi_y f d\vec{\xi}\right)_{y=y_3}. \tag{5}$$

From Eq. (5), we can derive the mass, momentum, and energy-conservation equations for both sides of Knudsen layer:

$$\rho_e \sqrt{\frac{RT_e}{2\pi}} - \rho_3 \sqrt{\frac{RT_3}{2\pi}} \beta F^- = \rho_3 u_3, \tag{6}$$

$$\frac{1}{2}\rho_e RT_e + \frac{1}{2}\rho_3 RT_3 \beta G^- = \rho_3 u_3^2 + \rho_3 RT_3, \tag{7}$$

$$2\rho_e RT_e \sqrt{\frac{RT_e}{2\pi}} - 2\rho_3 RT_3 \sqrt{\frac{RT_3}{2\pi}} \beta H^- = \frac{1}{2}\rho_3 u_3^2 \left(u_3^2 + 5RT_3\right), \tag{8}$$

where F^-, G^-, and H^- are

$$\begin{cases} m \overset{\text{def}}{=} \dfrac{u_3}{\sqrt{2RT_3}} = \sqrt{\dfrac{\gamma}{2}} \dfrac{u_3}{\sqrt{\gamma RT_3}} = \sqrt{\dfrac{\gamma}{2}} \text{Ma} \\ F^- = -\sqrt{\pi} m\, [1 - \text{erf}(m)] + \exp^{-m^2} \\ G^- = (2m^2 + 1)\, [1 - \text{erf}(m)] - \dfrac{2}{\sqrt{\pi}} \exp^{-m^2} \\ H^- = -\dfrac{\sqrt{\pi}}{2} m(m^2 + \dfrac{5}{2})\, [1 - \text{erf}(m)] \\ \qquad + \dfrac{1}{2}(m^2 + 2) \exp^{-m^2}, \end{cases} \tag{9}$$

where Ma is the Mach number at $y = y_3$ and erf(m) is the Gaussian error function. With the dimensionless variable m, Eq. (6)–(8) can be given as

$$\begin{cases} \sqrt{\dfrac{T_3}{T_e}} = \sqrt{1 + \dfrac{\pi}{64} m^2} - \dfrac{\sqrt{\pi}}{8} m \\ \dfrac{P_e}{P_3} = \dfrac{2 \exp^{-m^2}}{F^- + \sqrt{\frac{T_3}{T_e}} G^-} \\ \beta = \dfrac{2(2m^2 + 1)\sqrt{\frac{T_3}{T_e}} - 2\sqrt{\pi} m}{F^- + \sqrt{\frac{T_3}{T_e}} G^-} \end{cases}. \tag{10}$$

Based on the previous study [36], Ma cannot be larger than 1. Actually, there is no solution for the Boltzmann equation in Knudsen layer if the Mach number is larger than 1 [38,39]. Subsonic evaporation means Ma < 1 at $y = y_3$. Supersonic evaporation means Ma $= 1$ at $y = y_3$ and Mach number is larger than 1 in rarefaction fun, which is described later.

Essentially, the mass loss and recoil pressure are mass flux and momentum flux on the liquid surface. Based on the conservation equations, the mass loss and recoil pressure are given as

$$m_{\text{loss}} = \rho_3 u_3 = m\sqrt{\frac{2}{R}} \times \frac{P_3}{P_e} \times \frac{T_e}{T_3} \times \frac{P_e}{T_e}, \tag{11}$$

$$P_{\text{recoil}} = \rho_3 u_3^2 + \rho_3 RT_3 = \frac{P_e e^{m^2}}{2} (F^- + \sqrt{\frac{T_3}{T_e}} G^-) \times (2m^2 + 1). \tag{12}$$

According to the Clausius-Clapeyron relation, the saturated vapor pressure P_e is

$$\ln\left(\frac{P_e}{P_{\text{ref}}}\right) = -\frac{L_v}{R}\left(\frac{1}{T_e} - \frac{1}{T_{\text{ref}}}\right), \tag{13}$$

where T_{ref} and P_{ref} is the reference point on the saturated vapor temperature-pressure curve, for example, the boiling

temperature under the standard atmosphere pressure. L_v is the specific latent heat of evaporation for the material.

The only independent variable in Eq. (10) is Ma. Therefore, it is necessary to link the variables (pressure, temperature, and velocity) outside the Knudsen layer with those of ambient gas. In the following discussion, the flow field $y > y_3$ is taken to be steady.

2. Flows in common atmosphere

Knight [26] proposed flow structure outside the Knudsen layer shown in Fig. 2. The subsonic evaporation flow field is divided into four regions in Fig. 2(a): region I represents the ambient gas; region II represents the expanded vapor; region III represents the vapor flow caused by evaporation; region IV represents the Knudsen layer. There is a shock-wave discontinuity between the ambient gas and expanded vapor. The supersonic evaporation flow field, as shown in Fig. 2(b), is similar to the subsonic flow field except for the rarefaction fun between region IV and region III. In the supersonic flow regime, Ma $= 1$ at $y = y_3$ and vapor flow will accelerate in the rarefaction fun [26], which is a thin layer with rare gas molecules.

Knight [26] and Bellantone [40] made some assumptions to derive their evaporation models. However, their assumptions were either too complex or oversimplified. Here the assumptions for our evaporation model are listed as follows.

(i) There is a well-defined saturated pressure under a certain temperature for the metal.

(ii) The vapor and ambient gas are simplified as ideal gases (the viscosity is zero). In this way, Euler equations for nonviscous fluid are applied to our model for analytical solution. Meanwhile, the thermal conductivity and diffusion coefficient are assumed to be zero. It is addressed later in the evaporation model.

(iii) The plasma is ignored, considering the power density of the laser is not too high. Usually, the area energy density in the SLM process is about 10 MJ/m^2 [5] in the keyholing process, which is lower than that in laser welding (100–1000 MJ/m^2) [7].

(iv) The density and temperature in each gas-flow region is considered to be constant.

Moreover, the Mach number should be larger than 0.05, as suggested by Knight [26]. Under this condition, the convection dominates the mass transfer, so the diffusion and heat conduction between vapor and ambient gas could be ignored. For the keyhole regime in SLM, the velocity of vapor flow is comparable to the sound speed [41] and the Mach number is larger than 0.05, so the convection-flow regime is reasonable.

We assume that the vapor phase in region II is fully expanded throughout the shock-wave discontinuity. Therefore, the temperature T, pressure P, and velocity u satisfies

$$\begin{cases} P_2 = P_1 \\ T_2 = T_1 \\ u_2 = u_1 = 0. \end{cases} \tag{14}$$

The shock-wave discontinuity exists between region II and region III, as shown in Fig. 2(c). We use the coordinate fixed on the shock wave. Based on the Rankine-Hugoniot jump condition, the relationships between the variables of region II and region III are shown below.

$$\begin{cases} \dfrac{P_3}{P_2} = 1 + \dfrac{2\gamma}{\gamma+1}\left(M_2^2 - 1\right) \\ \dfrac{T_3}{T_2} = \left[1 + \dfrac{2\gamma}{\gamma+1}(M_2^2 - 1)\right]\dfrac{2 + (\gamma-1)M_2^2}{(\gamma+1)M_2^2} \\ \dfrac{u_2'}{u_3'} = \dfrac{u' - u_3}{u'} = \dfrac{2 + (\gamma-1)M_2^2}{(\gamma+1)M_2^2}, \end{cases} \tag{15}$$

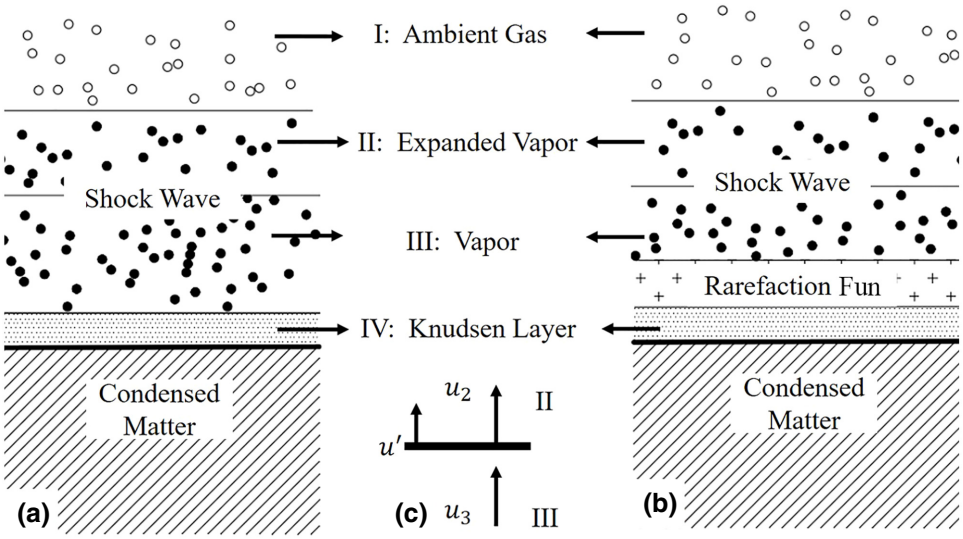

FIG. 2. Flow structure of the evaporation model. (a) Flow structure in common atmosphere. (b) Flow structure in near-vacuum atmosphere. (c) The scheme of shock wave bewteen region II and region III. The black solid circles represent the vapor molecules; the blank circles represent the ambient gas molecules.

where γ is the ratio of isochoric and isobaric specific heat capacity of the gas (for monoatomic gas $\gamma = 5/3$). $M_2 = u'/\sqrt{\gamma RT_2}$. u' is the velocity of shock wave shown in Fig. 2(c). Substituting Eq. (10) (equations on temperature and pressure ratio) into Eq. (15), the pressure and velocity relations across the shock wave can be rewritten as

$$\frac{P_e}{P_1} = \frac{P_e}{P_3} \times \frac{P_3}{P_2} = \frac{2\exp^{-m^2}}{F^- + \left(\sqrt{1+\frac{\pi}{64}} - \frac{\sqrt{\pi}}{8}m\right)G^-} \times \left(\frac{5}{4}M_2^2 + \frac{1}{4}\right), \quad (16)$$

$$\frac{3M_2^2 - 3}{4M_2^2} = \frac{m}{M_2} \times \frac{\sqrt{2RT_3T_e}}{\sqrt{\gamma RT_eT_1}} = \left(\sqrt{1+\frac{\pi}{64}} - \frac{\sqrt{\pi}}{8}m\right)\frac{m}{M_2}\sqrt{\frac{2T_e}{\gamma T_1}}, \quad (17)$$

where m and M_2 can be obtained by solving Eqs. (16) and (17). Therefore, the recoil pressure, mass flux, and energy flux can then be obtained.

Since the boiling point varies with metals, the composition of vapor phase is quite different from liquid alloy and R can not be treated as a temperature-independent variable. Theoretically, a $T_e - P_e$ curve tested by experiment should be obtained to solve this problem. To incorporate the compositions of the alloy in the evaporation model, we assume that the overall saturated pressure is proportional to the linear combination of each component's saturated pressure, similar to Raoult's law in physical chemistry. The saturated pressure P_e, molar mass M, and the specific gas constant R of the vapor are

$$P_e = \sum_i k_i P_i, \quad (18)$$

$$M = \frac{\sum_i M_i k_i P_i}{\sum_i k_i P_i}, \quad (19)$$

$$R = \frac{R_{\text{mol}}}{M}, \quad (20)$$

where M_i, k_i, and P_i are the molar mass, molar fraction, and saturated pressure of the ith component under specific temperature. $R_{\text{mol}} = 8.314$ J/(K mol). If the chemical bonds between different elements are much larger or smaller than the largest or smallest chemical bonds within individual elements in liquid phase, the assumption is not valid. For most alloys, such as Ti-6Al-4V and 304L, the assumption is suitable. In the current study, Ti-6Al-4V and 304L stainless steel are used in the keyhole dynamics simulation to prove that our evaporation model is widely applicable to different metal alloys. The mass fraction of compositions are listed in Table I, where the trace elements are ignored.

TABLE I. Element mass fraction.

	Mass fraction %					
	Ti	Al	V	Cr	Ni	Fe
Ti-6Al-4V	90	6	4			
304L stainless steel				18	8	74

An essential assumption of the flow structure is a continuous medium in regions II and III, which means the gas densities have lower thresholds in these regions. According to the study of Tsien [42], the Knudsen number K_n is a quantitative estimation of fluid rarefaction.

$$K_n = \frac{l}{L}, \quad (21)$$

where L is the characteristic length (the width of keyhole is about 150–500 μm). l is the mean free path of particles. To estimate the K_n of vapor phase, we assume that l is equal to the mean-free-path formula in equilibrium state. Therefore, the K_n of vapor phase can be given as

$$K_n = \frac{k_B T}{\sqrt{2}\pi d^2 PL}, \quad (22)$$

where d is the diameter of vapor molecule. T and P are the temperature and pressure of the vapor phase. Approximately, when $K_n < 0.01$, the gas can be treated as a continuous medium. When $0.01 < K_n < 0.1$, Navior-Stokes equations are still valid but slipping boundary condition should be applied. When $0.1 < K_n < 10$, it is the transitional flow regime, where collision and movement of particles are at the same scale. When $K_n > 10$, the collision among molecules can be ignored when compared with the motion of particles (also called "free-molecular-flow regime").

According to the derivation above, the ratio of pressure to temperature in each region has the following relation:

$$\frac{P_e}{T_e} > \frac{P_3}{T_3} > \frac{P_2}{T_2} = \frac{P_1}{T_1}. \quad (23)$$

Taking aluminum vapor for example, the diameter of aluminum molecule is 286 pm. The characteristic length L is about 1 mm in the SLM process. $K_n < 0.1$ in each region could be rewritten as

$$\frac{P_i}{T_i} > \frac{k_B}{0.1\sqrt{2}\pi d^2 L}. \quad (24)$$

Therefore, the usage criterion of the evaporation model for aluminum is

$$\frac{P_1}{T_1} > 0.3797. \tag{25}$$

When $T_1 = 298$ K, the range of ambient pressure is $P_1 > 120$ Pa. For other kinds of vapor, the scope of application is determined by Eq. (24). The d for alloys can be taken as the weighted average diameter of each particle.

3. Flow field in the near-vacuum environment

The near-vacuum environment represents the situation where $K_n \geq 0.1$. According to Ref. [43], the vapor flow transfers from free molecular flow to gas dynamic flow with the increase of laser-energy density in vacuum environment. In the gas-dynamic-flow regime, the Knudsen layer exists and Ma is equal to 1, which can be applied to calculate the mass loss and recoil pressure based on surface temperature. Actually, the vapor emitting from liquid surface will reach local equilibrium state after several collisions between molecules. In common ambient pressure, the region where nonequilibrium collision occurs is called Knudsen layer. In the near-vacuum environment, the Knudsen layer may not exist, especially in the conduction mode under vacuum environment, when Ma < 1.

To estimate the recoil pressure and mass loss in the near-vacuum environment, we propose an interpolation method based on the Mach number, Ma. The calculation steps are below.

(1) Use the evaporation model in Sec. II A 2 to obtain the liquid temperature range $[T_{k0}, T_{k1}]$, corresponding recoil pressure, and mass loss, where T_{k0} and T_{k1} represent the temperature when Ma are 0.05 and 1.

(2) If $T_{k1} < T_l$ (T_l is liquidus temperature), recoil pressure and mass loss can be obtained at different surface temperatures above T_l by substituting Ma $= 1$ into Eq. (12) and (11).

(3) If $T_{k0} < T_l < T_{k1}$, the result in step 1 with temperature T_l to T_{k1} is taken. When $T > T_{k1}$, the recoil pressure and mass loss at different surface temperatures is obtained by conservation Eqs. (12) and (11) with Ma $= 1$.

(4) If $T_l < T_{k0}$, recoil pressure and mass loss are calculated based on the model in Sec. II A 2.

Through the interpolation method, the recoil pressure and mass-loss functions are given in the near-vacuum environment. The result calculated from our model starts from the boiling point (boiling point varies under different ambient pressures). Actually, below the boiling point, the pressure on the liquid surface is equal to the ambient gas pressure and the influence of mass loss is extremely small, which can be ignored. Taking Ti-Al4-V as an example, with the decrease of ambient pressure, T_{k1}, T_{k0}, and boiling point decrease sharply. Under 1-atm ambient pressure, $[T_{k0}, T_{k1}]$ is about [3250, 4800 K] and boiling point is around 3200 K. Under 0.0002 atm ambient pressure, $[T_{k0}, T_{k1}]$ is about [2000 K, 2300 K] and boiling point is around 1950 K. The result consisting of strong evaporation is easier to calculate with the decrease of ambient pressure, if the energy density is constant.

It should be noted that our derived evaporation model is widely applicable to laser-, electron-beam-, and arc-based additive-manufacturing processes, and we take the SLM as an example. For electron-beam- and arc-based additive-manufacturing processes, the governing equations of the multiphysics thermal-fluid flow model are almost the same with the main difference being the heat-source model.

B. Multiphysics thermal-fluid flow model

In the multiphysics thermal-fluid flow model, the liquid phase is assumed to be Newton incompressible fluid with laminar flow. The mass-conservation equation is

$$\nabla \cdot \vec{v} = 0, \tag{26}$$

where $\vec{v}$ is the velocity vector. The momentum conservation equation is

$$\rho \frac{\partial \vec{v}}{\partial t} + \rho \nabla \cdot (\vec{v} \otimes \vec{v}) = -\nabla p + \mu \nabla^2 \vec{v} + \vec{f_B} + \rho \vec{g}, \tag{27}$$

where ρ and μ denote the mass density and dynamic viscosity taken as constant, and p is the pressure. The buoyancy force $\vec{f_B}$ is accounted for using the Boussinesq approximation, $\vec{f_B} = \rho \vec{g} \alpha_v (T - T_{\text{ref}})$, where $\vec{g}$ denotes the gravitational acceleration vector, α_v is the thermal expansion coefficient. The energy-conservation equation is

$$\rho \frac{\partial I}{\partial t} + \rho \nabla \cdot (\vec{v} I) = \nabla \cdot (k \nabla T) + q, \tag{28}$$

where k is the thermal conductivity, and T is the temperature. $I = C_p T + (1 - F_s) L_m$ is the specific internal energy, where C_p and L_m are the specific heat and specific latent heat of melting. q is the power absorbed by the material, which is incorporated by using the ray-tracing method [34] to track the multireflections of laser. In this model, the heat flux within the cross section of the laser beam is assumed to be a Gaussian distribution given as follows:

$$Q(x, y) = \frac{PN}{2\pi R_b^2} \exp\left(-N \frac{x^2 + y^2}{2R_b^2}\right). \tag{29}$$

The distribution of the heat source is determined by the laser power P, the concentration coefficient of laser beam N and the beam radius R_b. In the simulation, we define the beam radius containing 99% of the laser beam energy, thus N is set to be 4.6.

The ray-tracing model proposed by Ahn and Na [34] is implemented. The laser beam is subdivided into a series of subbeams and the absorption rate of each subbeam at each reflection is calculated by the Fresnel equation. In the current model, the reflection is assumed to be specular reflection. The complex refractive index of Ti-6Al-4V and 304L stainless steel, respectively, use titanium's [44] and iron's [44] complex refractive index instead due to the lack of reliable data.

The free surface of the molten pool is captured using the VOF method [33].

$$\frac{\partial f_l}{\partial t} + \nabla \cdot (f_l \vec{v}) = 0, \tag{30}$$

where f_l is the volume fraction. On the free surface, the pressure conditions are

$$p_s = \sigma(T)K + P_{\text{rec}}(T), \tag{31}$$

where K is the curvature of the free surface. $\sigma(T) = \sigma_0 - \sigma_s^T(T - T_m)$ and $P_{\text{rec}}(T)$ are the temperature-dependent surface-tension coefficient and recoil pressure. σ_0 and σ_s^T are surface tension coefficient at the reference temperature T_m and its temperature sensitivity. For the thermal boundary condition, it consists of heat convection, heat radiation, and heat loss of evaporation [32]

$$-k\nabla T \cdot \vec{n} = h(T - T_{\text{sur}}) + \epsilon\sigma_s(T^4 - T_{\text{sur}}^4) + m_{\text{loss}}L_v, \tag{32}$$

where $\vec{n}$, σ_s, and T_{sur} are the normal vector to the interface, the Stefan-Boltzmann constant [5.6704×10^{-8} W/(m^2 $\times$ K^4)] and the ambient temperature, respectively.

It should be noted that the powder motion is not incorporated in the current multiphysics model, which is a tough problem in the SLM simulation. Chen and Yan [45] have developed a gas-particle multiphase flow model for the powder spattering and denudation during the SLM process. However, the complex interactions between the molten-pool dynamics, powder motions, and gas dynamics should be further studied with more comprehensive models. Moreover, the laser defocusing is not considered in the current multiphysics model. It is demonstrated that the focal length has effects on the power density and consequently microstructure [46], which requires further systematic investigation.

III. RESULTS AND DISCUSSION

A. Mass loss and recoil pressure

The mass-loss (evaporation) coefficient is the ratio of the net to maximum mass loss of evaporation. Based on Eq. (6), the mass-loss ratio is

$$M_{\text{co}} = \frac{\rho_3 u_3}{\rho_e \sqrt{\frac{RT_e}{2\pi}}} = 1 - \frac{P_3}{P_e}\sqrt{\frac{T_e}{T_3}}\beta F^-. \tag{33}$$

Combining Eq. (9), (10), and (33) indicates the evaporation coefficient is determined by the Ma. In Fig. 3(a), the evaporation coefficient of Ti-6Al-4V under common atmosphere tends to 0.82 with the increase of Ma, which is consistent with the evaporation models by Anisimov [27] and Klassen [18]. In addition, Fig. 3(b) shows that Ma linearly increases with surface temperature, which agrees with Klassen's conclusion [18]. Although the Mach number of the shock-wave nonlinearly increases with the liquid metal temperature as shown in Fig. 3(b), it has nearly no influence on the mass loss. That means, the flow structure outside the Knudsen layer has little effect on mass loss.

In 1915, Knudsen [24] found that the maximal evaporation rate only occurred in highly purified mercury and the impure mercury evaporation rate was lower. To explain the lower evaporation rate, he introduced an evaporation coefficient α, which is between 0 and 1. The most commonly used recoil pressure function is based on Anisimov's

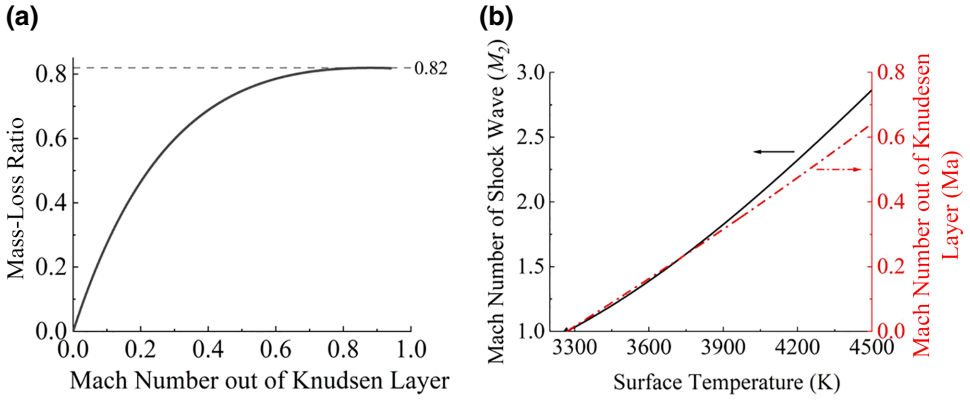

FIG. 3. Mass-loss ratio and Mach number in 1 atm for Ti-6Al-4V. (a) Mass-loss ratio with match number out of Knudsen layer; (b) Mach number under different surface temperature.

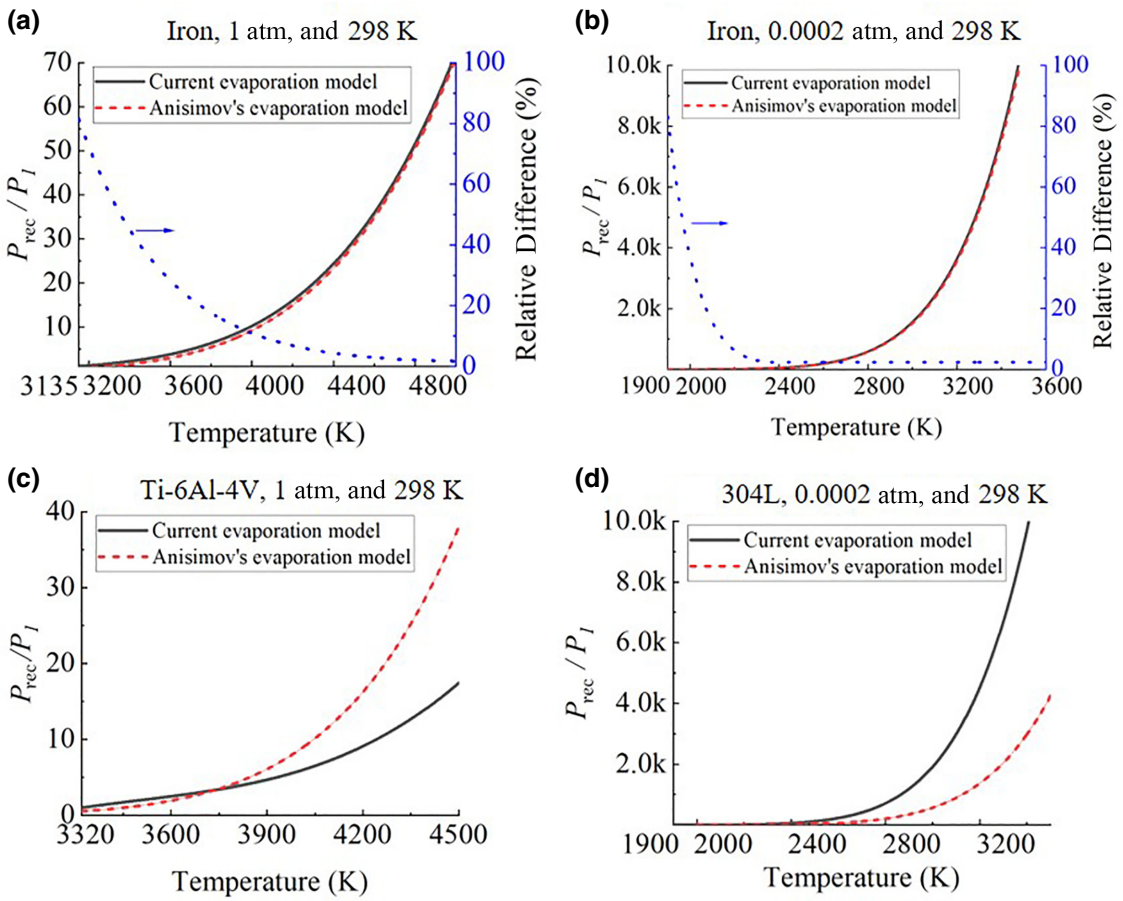

FIG. 4. Recoil pressure ratio at different molten-pool surface temperature. (a) Evaporation of iron under 1-atm and 298-K environment. (b) Evaporation of iron under 0.0002-atm and 298-K environment. (c) Evaporation of Ti-6Al-4V under 1-atm and 298-K environment. (d) Evaporation of 304L stainless steel under 0.0002-atm and 298-K environment. Black solid line: current evaporation model. Red dashed line: Anisimov's evaporation model. Blue dashed line: the relative difference. (The starting points in the figures are the boiling point of the materials.)

evaporation model.

$$P_{\text{rec}} = \alpha P_b \exp\left(L_v \frac{T - T_b}{RTT_b}\right), \tag{34}$$

where P_b is the saturated pressure at T_b. Anisimov assumed that the bulk velocity of vapor at $y = y_3$ is at local sound speed, so α is equal to 0.54 [27].

The recoil pressure ratio is the ratio of recoil pressure to ambient pressure. Figures 4(a) and 4(b) show the influence of ambient pressure in the evaporation model of pure iron. The recoil pressure of the two models have similar tendency and the recoil pressure of our model is larger than that of Anisimov's model when Ma < 1. The recoil pressure ratio in our model is larger than 1 when $T > T_b$, while the ratio in Anisimov's model is lower than 1 when $T_b < T < T_{m1}$ (T_{m1} is the temperature when recoil pressure ratio is equal to 1 based on Anisimov's model), which is not reasonable in physics. Actually, the influence of ambient pressure is not incorporated in Anisimov's model, which impedes the expansion of vapor and increases the recoil pressure. For pure metal, the difference between the two models is relatively small when the recoil pressure ratio is much larger than 1, which means evaporation is strong enough and the influence of ambient pressure can be ignored.

Figures 4(c) and 4(d) show the influence of material compositions in the evaporation model. In Fig. 4(c), for Ti-6Al-4V under 1-atm and 298-K ambient environment, the recoil pressure ratio of Anisimov's model is smaller than that of the current model at the surface temperature ranging between 3315–3800 K, which is consistent with the discussion above. However, the recoil pressure in Anisimov's model is obviously higher when surface temperature is larger than 3800 K. In Fig. 4(d), for 304L stainless steel under 0.0002-atm and 298-K ambient environment, the recoil pressure ratio of our evaporation model is higher than Anisimov's model above the boiling point.

The difference between the two evaporation models of alloys is due to the $T_e - P_e$ curve. Rigorously speaking,

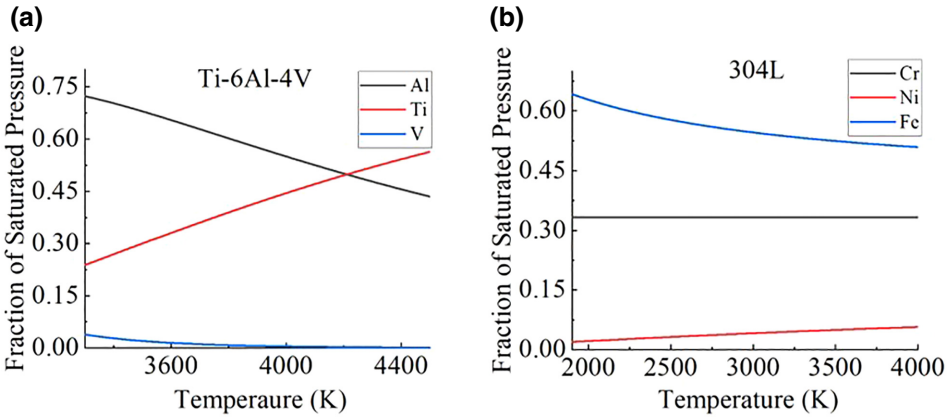

FIG. 5. Fraction of saturated pressure for different elements. (a) Ti-6Al-4V; (b) 304L stainless steel.

the Clausius-Clapeyron equation with fixed R and L_v is only suitable for materials whose vapor compositions do not change with temperature. Generally, L_v and T_b for alloys are obtained by experiment in 1-atm environment. Therefore, in Anisimov's evaporation model, it is assumed that the vapor composition at difference temperatures is the same as that at T_b under 1-atm environment.

However, some EBM experiments [47,48] show that the final compositions of TiAl-based alloy vary with different electron-beam energy density, which means the vapor compositions vary with the surface temperature. Figures 5(a) and 5(b) are the fraction of saturated pressure for Ti-6Al-4V and 304L stainless steel by our derived evaporation model, respectively. According to Eq. (12) and Fig. 5, the recoil pressure of the current evaporation model is proportional to the saturated pressure and the fraction of saturated pressure of each component differs with surface temperature. Taking Ti-6Al-4V for example, Al and Ti are the components that mainly contribute to the saturated pressure. The L_v and T_b of Al is smaller than that of Ti under 1-atm environment. The fraction of saturated pressure of Al decreases with the increase of surface temperature, which means a larger proportion of energy is used to overcome the latent heat of evaporation of Ti. Therefore, the $T_e - P_e$ curve of Ti-6Al-4V in our model is closer to the $T_e - P_e$ curve of Ti as the temperature increases. However, in Anisimov's model, the vapor compositions are assumed to be the same as those at the boiling point T_b under 1-atm environment. Therefore, compared with the current model, a larger proportion of Al is assumed to evaporate from the liquid surface when temperature increases and P_e is larger than P_e of the current model due to the larger saturated pressure of Al, according to the Clausius-Clapeyron equation of pure metal.

B. Experimental validation: stationary laser melting in common environment

To validate the derived evaporation model in common environment, the laser-induced keyhole-dynamics simulation is conducted and compared with published x-ray imaging results [5]. In the simulation, the material is Ti-6Al-4V, and the physical properties are listed in Table II. The ambient gas is 1 atm and 298 K. The laser

TABLE II. Material properties [18,21,32,49].

Property	Ti-6Al-4V	304L stainless steel
Solidus temperature (T_s)	1878 [K]	1697 [K]
Liquidus temperature (T_l)	1928 [K]	1727 [K]
Boiling temperature (T_b)	3315 [K]	2009 [K]
Solidus density (ρ)	4400 [kg/m^3]	7200 [kg/m^3]
Latent heat of melting (L_m)	2.86×10^5 [J/kg]	2.74×10^5 [J/kg]
Latent heat of evaporation (L_v)	9.7×10^6 [J/kg]	6.36×10^6 [J/kg]
Saturated vapor pressure (P_e)	1.013×10^5 [Pa] ($T_b = 3315$ K)	20.16 [Pa] ($T_b = 2009$ K)
Solidus-specific heat (c_s)	570 [J/(K·kg)]	712 [J/(K·kg)]
Liquidus-specific heat (c_l)	831 [J/(K·kg)]	837 [J/(K·kg)]
Thermal conductivity at solidus (k_s)	16 [W/(m·K)]	19.2 [W/(m·K)]
Thermal conductivity at liquidus (k_l)	32 [W/(m·K)]	22 [W/(m·K)]
Surface radiation coefficient (ϵ)	0.4	0.4
Surface tension coefficient (σ_0)	1.68 [N/m]	1.76 [N/m]
Temperature sensitivity of σ (σ_s^T)	0.00026	0.00043
Viscosity (μ)	0.005 [Pa·s]	0.006 [Pa·s]

TABLE III. Laser parameters in stationary laser-melting simulation.

Property	Common ambient pressure Value	Near-vacuum ambient pressure Value
Spot size	140 μm	100 μm
Wavelength	1070 nm	1070 nm
Power	156 W	260 W

parameters are listed in Table III, which are the same as the experiment setting. In the simulation, the mesh size is 4 μm to ensure accuracy. The computation time for one typical case is about 24 h on a desktop with an Intel I9-9900 CPU.

To exclude the effect of laser scanning on the keyhole formation, the x-ray imaging results of the stationary laser melting by Cunningham *et al.* [5] is adopted to validate the current evaporation model in common environment. The keyhole formation process by the x-ray imaging experiment [5] and the two evaporation models at common ambient pressure are shown in Fig. 6. The figures with the serial number "A" are the x-ray images by Cunningham *et al.* [5], and "B" and "C" are the simulation results with the current evaporation model and Anisimov's evaporation model, respectively. According to Cunningham *et al.* [5], the molten-pool evolution process is divided into five stages: (1) melting; (2) vapor depression formation and growth; (3) vapor depression instability and periodic fluctuation; (4) keyhole formation and growth; (5) molten-pool shape change. In the experiments, the timing of the shutters versus the arrival of the laser light is not determined, which affects the real zero time of the laser-melting recording. Thus we track keyhole dynamics from the depression formation and growth stage, as shown in Fig. 6(A1), i.e., setting the starting time of the depression as the time zero.

In the depression formation and growth stage, x-ray images and simulations results match well. The keyhole depth in the experiment grows from 30 to 45 μm in 165 μs. Both simulations share the same trend and the depths increase from 30 to 80 μm in 90–100 μs. Since the laser absorptivity of aluminum is smaller than titanium, the complex refractive index of Ti-6Al-4V taken as titanium's [44] leads to larger laser absorptivity. Moreover, the diameter of laser varies with the depth of keyhole, but the defocusing is not incorporated in the multiphysics model. Thus the simulated growth rate of the keyhole is higher than that in the experiment.

After the depression formation and growth stage, the keyhole fluctuates, as shown in Figs. 6(A2)–6(A5). In this period, the shape of the keyhole keeps stable but the bottom vibrates. The x-ray images show that the period and amplitude of the fluctuation are about 10 μs and 12 μm. The period and amplitude of the current model are 12 μs and 12 μm, which agree well with the experiment. However, the keyhole fluctuation in Anisimov's evaporation model is not obvious. The period and amplitude of the vibration are about 10 μs and 4 μm, respectively. It might be that recoil pressure of Anisimov's evaporation model is higher and suppresses the fluctuation of the bottom of keyhole.

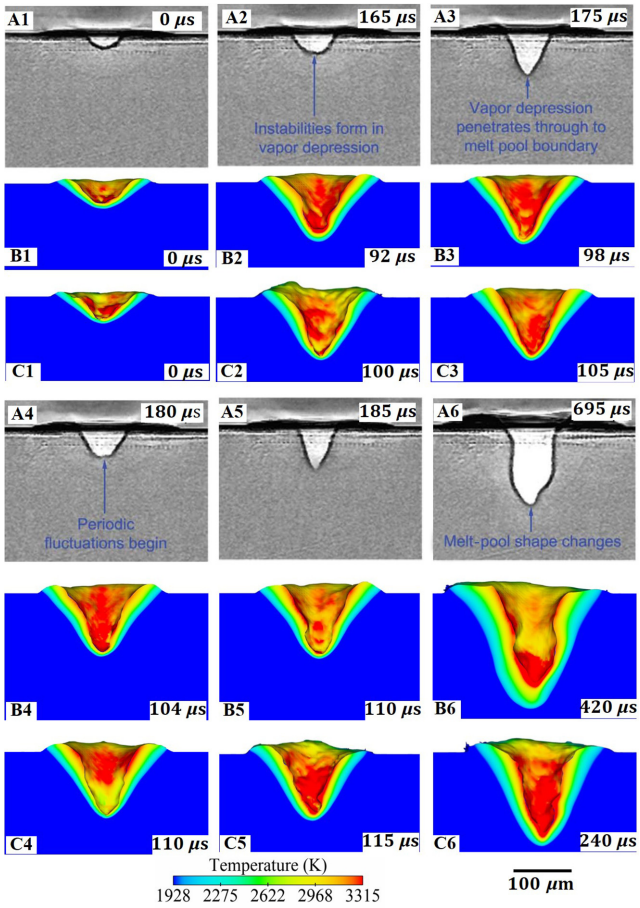

FIG. 6. Comparison of molten pool and keyhole at different time frames in stationary laser melting under 1-atm and 298-K environment. (A1)–(A6) X-ray images of keyhole shapes [5]; (B1)–(B6) simulated keyhole shapes with current evaporation model; (C1)–(C6) simulated keyhole shapes with Anisimov's evaporation model. (Experimental figures are from [5], reprinted with permission from AAAS.)

In the next stage, the shape of keyhole starts changing and penetrates further. The increasing depth of keyhole is shown in Fig. 7(a). The trend of the x-ray experiments and simulations are different. In Figs. 6(A6), 6(B6), and 6(C6), the keyhole penetrates to about 146 μm. In the experiment, the keyhole fluctuates in this depth range for about 270 μs. In the current recoil model, it lasts about 180 μs, obviously longer than that of Anisimov's evaporation model, which is about 110 μs. The relative difference of Anisimov's evaporation model to the experimental results is about 59%

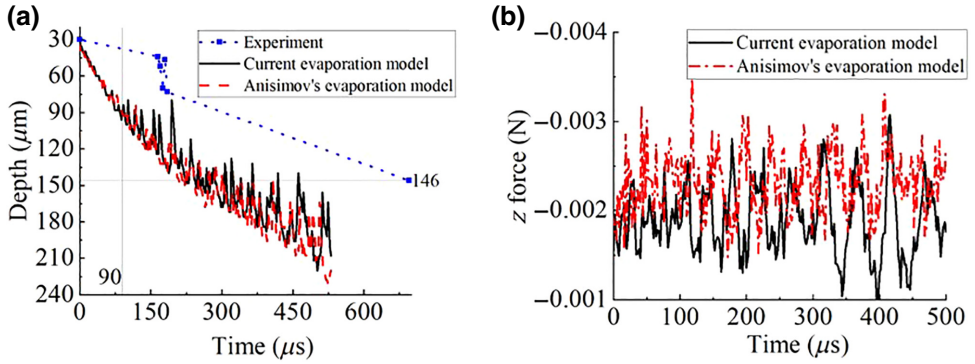

FIG. 7. Comparison of (a) the keyhole depth (the blue dashed line is the depth-growing trend. The time zero is the starting time of the depression stage. In the simulations, the keyhole starts fiercely fluctuating around 90 μs. In the x-ray imaging observation, the keyhole depth starts fiercely fluctuating at 185 μs) and (b) z-direction recoil force on the keyhole surface for SLM under 1-atm and 298-K environment.

much higher than that of current evaporation, 30%. Different from experiment, the laser beams in the simulations are parallel without defocusing effect, which leads to higher-energy concentration in the bottom of the keyhole and increases the keyhole-depth growth speed. The keyhole formation process of the two evaporating models show that our derived evaporation model matches better with the x-ray imaging results while Anisimov's model is fiercer and nearly omits the transition period.

Comparing the keyhole-depth [Fig. 7(a)] evolution, it shows that the depth fluctuation in Anisimov's model is not fiercer than the current model, which is different from the tendency in the experiment of Cunningham [5]. Moreover, the depth-penetrating process of Anisimov's model is faster than the current model. The differences between the simulation results and experimental observation could be the results of neglecting some physical factors, e.g., the laser defocusing, alloy oxidation, and plume etc. These factors would decrease the energy absorption and lower the energy concentration as the depth of molten pool grows in the experiment. Moreover, the depth of keyhole before the formation and growth stage increases steadily, while it fluctuates fiercely after 185 μs. In Fig. 7(a), the depth evolution from x-ray imaging result after 185 μs mainly represents the keyhole-depth growing trend. This fierce fluctuation is due to the local energy concentration at the bottom of the keyhole and instant energy release, which results in the sudden change of keyhole shape and liquid spattering. Zhao *et al.* [50] named this phenomenon bulk explosion, which cannot be simulated with the current multiphysics model.

We further compare the keyhole-surface recoil force along the z direction F_z changing with time in Fig. 7(b).

$$F_z = \int_\Gamma P_z dS, \tag{35}$$

where P_z is the z component of recoil pressure, and Γ is the keyhole-surface area.

Note that the recoil pressure is along the z direction, thus its value is negative. In the penetration period, the average F_z of Anisimov's evaporation model is about -2.3×10^{-3} N, while the current evaporation model is about -1.9×10^{-3} N, 17% lower in absolute value. The F_z deviation of Anisimov's evaporation model and current evaporation model are similar, which are -3.69×10^{-4} N and -3.94×10^{-4} N, respectively. Furthermore, there is no obvious increase of recoil force as the keyhole becomes deeper. It indicates that the F_z has remarkable influence on the keyhole deepening rate but minor influence on the keyhole shape in common environment.

We analyze the diameter of molten pool and overflowing metal above the surface (Fig. 8) at 600 μs in simulations. The results show that diameter by the current evaporation model and Anisimov's evaporation model are 312 μm and 296 μm, respectively. The depth by current evaporation model and Anisimov's evaporation model are 200 μm and 220 μm, respectively. However, the metal overflow [see the dashed rectangle of Figs. 8(c) and 8(d) are different]. The height of overflowing liquid above the base plate of Anisimov's evaporation model is 34 μm, more than 20% higher than 26 μm of our derived model, while x-ray images do not show obvious overflowing. The darker area in the x-imaging results is due to the difference of the refractive index near the surface, which is not overflowing. The recoil force not only enhances the penetrating speed, but also aggregates liquid-metal overflowing in Anisimov's evaporation model in common environment.

C. Experimental validation: stationary laser melting in near-vacuum environment

Currently, the SLM process under a near vacuum [51–53] is a research direction in additive manufacturing.

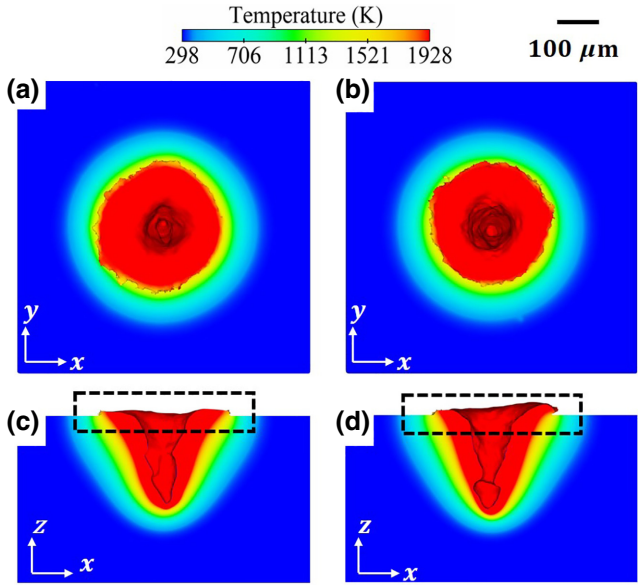

FIG. 8. Shape of the molten pool at $t = 600$ μs. (a),(b) Top view of the molten pool of the current evaporation model and Anisimov's evaporation model; (c),(d) cross section of the molten pool of the current evaporation model and Anisimov's evaporation model.

It is proven that the SLM under a near-vacuum environment can reduce the oxidation of samples compared with the common gas environment. To study the keyhole formation in a near-vacuum environment and validate the current evaporation model for different materials, a simulation of stationary laser-induced keyhole dynamics on the 304L stainless steel base plate is conducted. The simulation parameters are the same as the experiment by Guo *et al.* [12]. The physical parameters of the base plate and laser parameters are given in Tables II and III. Ambient gas is 0.0002 atm and 298 K. The Knudsen number Kn $\approx 7 > 0.1$ and the evaporation model in near-vacuum environment is used.

According to the experiment, about 120 powder particles spatter above the powder bed, the average diameter of the powder particle is 35 μm, and the powder-bed thickness is 136 μm. From the experimental figures, we can estimate the spattering powder particles are mostly from a circular region of 220 μm in diameter surrounding the laser spot. Given the relative packing density of the powder bed around 50% [54], we can approximate most of the powder particles in that region are blown off. Therefore, we can assume that laser energy is deposited on the base plate in the simulations.

The keyhole formation process by x-ray imaging experiment [12] and the simulation results of two evaporation models are given in Fig. 9. The numbering method of Fig. 9 are the same as Fig. 6: "A" for the x-ray imaging experiment, "B" for the current evaporation model, "C" for

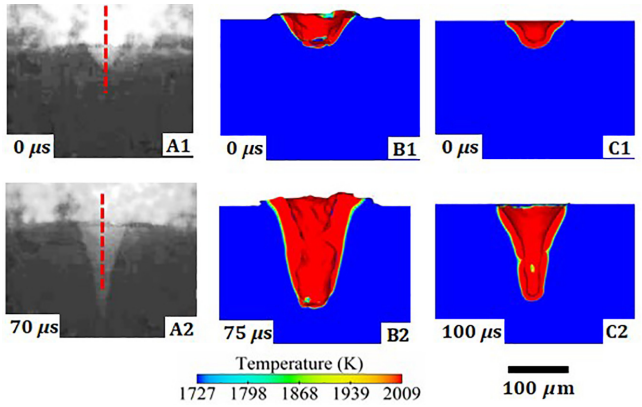

FIG. 9. Comparison of molten pool and keyhole in stationary laser melting under 0.0002-atm and 298-K environment. (A1),(A2) X-ray images of keyhole shapes [12] and the red dashed line indicates the laser position; (B1),(B2) simulated keyhole shapes with the current evaporation model; (C1),(C2) simulated keyhole shapes with Anisimov's evaporation model. (Experimental figures are reprinted from [12] with permission from Elsevier.)

Anisimov's evaporation model. We set the same starting time as that in the simulations in common environment, i.e., the depression formation and growth stage, to track the keyhole dynamics. The depth of keyhole below the substrate surface is about 32 μm at the start.

In Figs. 9(A1) and 9(A2), it takes 70 μs for the depth of the keyhole below the substrate surface to grow from 32 μm to 136 μm. For the current and Anisimov's evaporation model, the periods are 75 μs and 100 μs as shown in Figs. 9(B2) and 9(C2). The relative time errors of the current and Anisimov's evaporation model during this period are 7% and 43%, respectively. Our derived evaporation model is much closer to the experiment, while Anisimov's evaporation model is quite different.

The recoil pressure distribution on the keyhole surface of Figs. 9(B2) and 9(C2) are shown in Figs. 10(a) and 10(b), respectively. The highest recoil pressure of both evaporation models are about 5 atm at the bottom of the

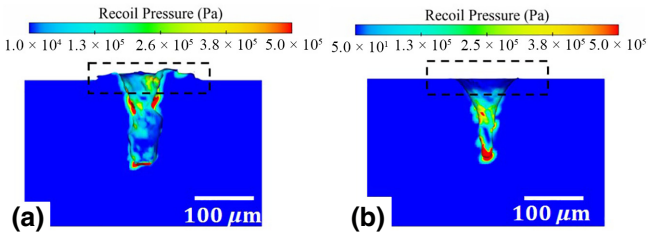

FIG. 10. Recoil pressure distribution on the keyhole surface under 0.0002-atm and 298-K environment. (a) Current evaporation model at 75 μs. (b) Anisimov's evaporation model at 100 μs.

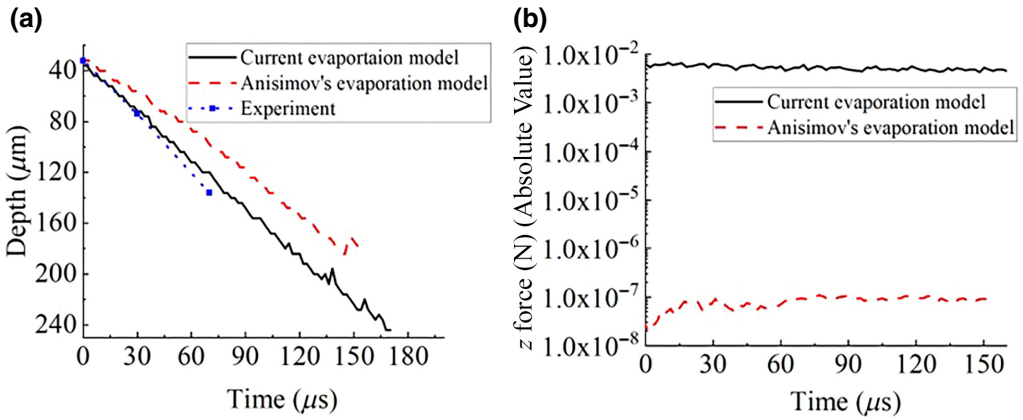

FIG. 11. Comparison of (a) the keyhole depth and (b) z-direction recoil force on keyhole surface for SLM under 0.0002-atm and 298-K environment. Black solid line for the current evaporation model. Red dashed line for Anisimov's evaporation model.

keyhole, but the recoil pressure distributions of the evaporation models are very different. On the edge of the keyhole, the recoil pressure of the current evaporation model is higher than 0.1 atm, while the recoil pressure in Anisimov's evaporation model is less than 0.0005 atm, as shown in the black dashed box of Fig. 10. In the experiment [12], there is obviously an overflowing phenomena on the edge of the keyhole. The height of the keyhole above the substrate is about 18 μm. In our derived evaporation model, the keyhole height above the keyhole is about 14 μm. In contrast, almost no overflowing occurs when using Anisimov's model. Actually, the mass-loss rate of Anisimov's model is much larger than our model around the boiling point under 0.0002-atm ambient pressure. Therefore, the amount of liquid is smaller on the wall of the keyhole and the amount of liquid that could be pushed out as overflow is smaller than Anisimov's evaporation model's result.

Although the keyhole depth variation below the base plates for the two evaporation models are similar [as shown in Fig. 11(a)], the absolute value of z-direction recoil force in the current evaporation model is much higher as shown in Fig. 11(b). The z-direction recoil force in the current evaporation model is about 4×10^{-3} N, while it is about 8×10^{-8} N in Anisimov's evaporation model. Assuming the force on particles equal to z-direction recoil force and the contacting time is 70 μs, the maximum impulses on spattering particles by the current and Anisimov's evaporation model are 2.8×10^{-7} kg m/s and 5.6×10^{-12} kg m/s, respectively. In the experiment, the average mass of the powder particle is about 1.5×10^{-10} kg. The velocity of 120 spattering powder particles is about 1 m/s. The total momentum of the spattering particles is 1.8×10^{-8} kg m/s, which is much larger than the impulse by Anisimov's evaporation model and comparable to the current evaporation model. This further demonstrates the validity of our evaporation model, as well as the drawback of Anisimov's model.

As discussed in Sec. III A, Anisimov's evaporation model ignored the influence of material composition on the saturated pressure. For 304L stainless steel, Fe, Ni, and Cr all contribute to the change of saturated pressure, as shown in Fig. 5(b). In Anisimov's model, the vapor compositions at different surface temperatures are assumed to be the same as those at T_{b1}, the boiling point of 304L at 1 atm. The saturated pressure of the component with lower T_{b1} and L_v increases more rapidly than that of other components, with the increase of surface temperature. Therefore, the saturated pressure in the current model is larger than Anisimov's model, when the evaporation is strong enough (for example, $T_e > T_{k1}$). The simulation results of current evaporation model show that the keyhole depth is closer to experiment results, which validates this assumption.

D. Experimental validation: laser scanning in common environment

To understand the physical mechanism of the keyhole dynamics during the laser-scanning process, we simulate single-track laser scanning with the current evaporation model on Ti-6Al-4V. The ambient gas is 1 atm and 298

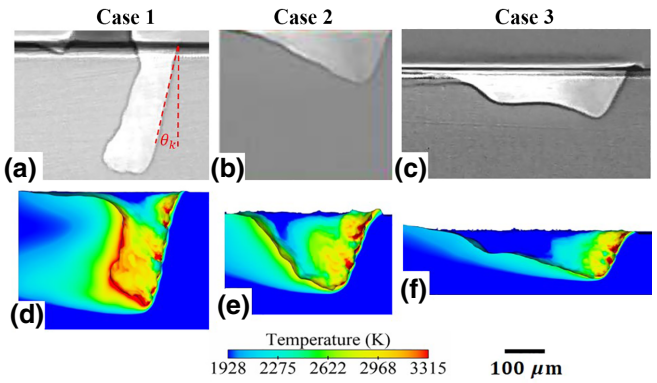

FIG. 12. Comparison of the keyhole geometry feature of current model with the experimental results. (a)–(c) X-ray images of keyhole shape [5]; (d)–(f) simulated keyhole shapes and temperature distribution. The inclination angle θ_k is the angle of front wall with z direction shown in (a). (Experimental figures are from [5], reprinted with permission from AAAS.)

TABLE IV. Comparison of the keyhole geometry feature of the current model with the experimental results [5].

Geometry feature		Case 1 700 mm/s	Case 2 1200 mm/s	Case 3 1500 mm/s
Average depth $\overline{d}_k$ (μm)	Experiment	$\sim$ 320	$\sim$ 163	$\sim$ 130
	Simulation	$\sim$ 330	$\sim$ 185	$\sim$ 147
Average inclination degree $\overline{\theta}_k(^\circ)$	Experiment	$\sim$ 11	$\sim$ 20	$\sim$ 25
	Simulation	$\sim$ 14	$\sim$ 19	$\sim$ 23

K. The laser parameters are 416 W of power and 95 μm of spot diameter with three different scanning speeds: 700 mm/s (case 1), 1200 mm/s (case 2), and 1500 mm/s (case 3), as in the x-ray imaging experiments [5].

In Fig. 12, the simulation results of keyhole shape of three simulation cases are consistent with the experimental results in Ref. [5]. Table IV shows the average depth and inclination angle of the keyhole. The maximum relative difference of depth and inclination are 14% and 22%, while the absolute differences are 22 μm and 3°, which is in good agreement with experiments. The molten-pool length and depth of the current multiphysics model also prove to match well with the experimental results in our previous work [55]. The maximum difference of keyhole length is around 45 μm in case 1, and the relative difference is about 37%, which is due to the fluctuation of the back wall of the keyhole. A little fluctuation of the back wall leads to dozens of micrometers' change of length. The temperature distribution on the back wall of the keyhole shows that the evaporation is not obvious and the z-direction recoil force is much smaller compared with that on the front wall at high laser scanning speed. The Marangoni force along the keyhole surface is the main driving force for the back-wall motion, especially the relatively shallow and long keyhole. In the current multiphysics model, the Marangoni force only accounts for the temperature gradient without the influence of composition gradient. In the first two cases, the disagreements of keyhole morphology between the simulation and experiment are larger than that of the third case. The energy absorptivity is higher in the first two cases, which leads to fiercer thermal flow and metal evaporation. Therefore, the composition gradient is larger, the neglect of which results in the disagreement.

In the first simulation case, the rear keyhole wall is hotter than the front keyhole, which is different from the other two simulation cases. Since the rear part of keyhole in the first case is not directly exposed to the ambient gas but shaded by the molten fluid in both the experiment and simulation, this kind of keyhole shape traps more laser rays and thus leads to a higher-energy absorption and a higher temperature on the rear keyhole wall. Moreover, the recoil pressure on the rear keyhole wall should be strong enough to hold the overhanging shape of the rear keyhole, otherwise it would collapse. Therefore, the temperature on the rear keyhole wall is higher than that on the front keyhole wall in the first simulation case.

To further analyze the keyhole fluctuation, the laser-energy absorption and recoil forces are given in Fig. 13. The absorptivity of Ti-6Al-4V decreases from about 78% to 65% as the scanning speed increases from 0.7 m/s to 1.5 m/s Although the total energy absorptivity [Fig. 13(a)] decreases with the increase of scanning speed, the total energy absorptivity on the front wall of the keyhole [Fig. 13(b)] remains stable around 22%. It indicates that the front wall of the keyhole mainly absorbs the energy in the first reflection, and the bottom and back wall of the keyhole experience the following multiple reflections. In Fig. 13(c), the total recoil force along the z direction

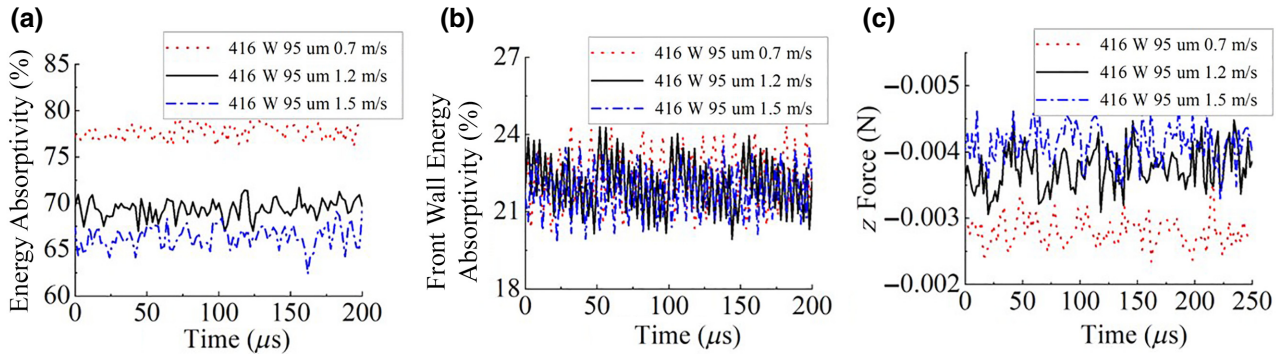

FIG. 13. Comparison of the keyhole energy distribution and z-direction recoil force of three cases. (a) The total keyhole energy absorptivity; (b) the keyhole front wall total energy absorptivity including first incident and subsequent reflections; (c) the total recoil force along the z direction.

increases with the scanning speeds. Comparing the shape of keyhole in Fig. 12, the area of keyhole surface increases with the scanning speed is the main reason for the increase of the z-direction recoil force. In other words, although the energy absorptivity decreases with the increase of laser-scanning speed, the z-direction recoil force increases under the same laser power.

IV. CONCLUSIONS

An evaporation model considering the influence of ambient gas and material composition is developed and successfully implemented in a multiphysics thermal-fluid flow-simulation model. The analysis of the evaporation model indicates that material composition and ambient environment play roles in recoil pressure and mass-loss rate, especially in a near-vacuum environment.

Validating against the x-ray imaging results of keyhole dynamics, the keyhole simulations demonstrate that Anisimov's evaporation model is only applicable when evaporation is strong enough, while our evaporation model is reasonable under different surface temperatures and ambient pressures. Moreover, the results indicate that our evaporation model is widely applicable to different material compositions, while Anisimov's evaporation model is only suitable for pure materials. Furthermore, the analysis of the temperature distribution, energy distribution, recoil pressure, and z-direction recoil force on the keyhole provides more thorough understanding of the physical mechanisms and further guidance to control the keyhole dynamics.

ACKNOWLEDGMENTS

The authors acknowledge the financial support of Singapore Ministry of Education Academic Research Fund Tier 1.

L. Wang and Y. Zhang contributed equally to this work.

[1] L. Yang, O. Harrysson, H. West, and D. Cormier, Compressive properties of Ti-6Al-4V auxetic mesh structures made by electron beam melting, Acta Mater. **60**, 3370 (2012).

[2] W. Yan, W. Ge, J. Smith, S. Lin, O. L. Kafka, F. Lin, and W. K. Liu, Multi-scale modeling of electron beam melting of functionally graded materials, Acta Mater. **115**, 403 (2016).

[3] R. Rai, J. W. Elmer, T. A. Palmer, and T. DebRoy, Heat transfer and fluid flow during keyhole mode laser welding of tantalum, Ti-6Al-4V, 304 L stainless steel and vanadium, J. Phys. D: Appl. Phys. **40**, 5753 (2007).

[4] W. E. King, H. D. Barth, V. M. Castillo, G. F. Gallegos, J. W. Gibbs, D. E. Hahn, C. Kamath, and A. M. Rubenchik, Observation of keyhole-mode laser melting in laser powder-bed fusion additive manufacturing, J. Mater. Process. Technol. **214**, 2915 (2014).

[5] R. Cunningham, C. Zhao, N. Parab, C. Kantzos, J. Pauza, K. Fezzaa, T. Sun, and A. D. Rollett, Keyhole threshold and morphology in laser melting revealed by ultrahigh-speed x-ray imaging, Science **363**, 849 (2019).

[6] I. Eriksson, J. Powell, and A. F. H. Kaplan, Melt behavior on the keyhole front during high speed laser welding, Opt. Lasers Eng. **51**, 735 (2013).

[7] S. Li, G. Chen, M. Zhang, Y. Zhou, and Y. Zhang, Dynamic keyhole profile during high-power deep-penetration laser welding, J. Mater. Process. Technol. **214**, 565 (2014).

[8] C. Qiu, C. Panwisawas, M. Ward, H. C. Basoalto, J. W. Brooks, and M. M. Attallah, On the role of melt flow into the surface structure and porosity development during selective laser melting, Acta Mater. **96**, 72 (2015).

[9] P. Bidare, I. Bitharas, R. M. Ward, M. M. Attallah, and A. J. Moore, Fluid and particle dynamics in laser powder bed fusion, Acta Mater. **142**, 107 (2018).

[10] M. J. Matthews, G. Guss, S. A. Khairallah, A. M. Rubenchik, P. J. Depond, and W. E. King, Denudation of metal powder layers in laser powder bed fusion processes, Acta Mater. **114**, 33 (2016).

[11] C. Zhao, K. Fezzaa, R. W. Cunningham, H. Wen, F. De Carlo, L. Chen, A. D. Rollett, and T. Sun, Real-time monitoring of laser powder bed fusion process using high-speed x-ray imaging and diffraction, Sci. Rep. **7**, 3602 (2017).

[12] Q. Guo, C. Zhao, L. I. Escano, Z. Young, L. Xiong, K. Fezzaa, W. Everhart, B. Brown, T. Sun, and L. Chen, Transient dynamics of powder spattering in laser powder bed fusion additive manufacturing process revealed by in-situ high-speed high-energy x-ray imaging, Acta Mater. **151**, 169 (2018).

[13] L. I. Escano, N. D. Parab, L. Xiong, Q. Guo, C. Zhao, K. Fezzaa, W. Everhart, T. Sun, and L. Chen, Revealing particle-scale powder spreading dynamics in powder-bed-based additive manufacturing process by high-speed x-ray imaging, Sci. Rep. **8**, 15079 (2018).

[14] A. A. Martin, N. P. Calta, J. A. Hammons, S. A. Khairallah, M. H. Nielsen, R. M. Shuttlesworth, N. Sinclair, M. J. Matthews, J. R. Jeffries, T. M. Willey, and J. R. I. Lee, Ultrafast dynamics of laser-metal interactions in additive manufacturing alloys captured by in situ x-ray imaging, Mater. Today Adv. **1**, 100002 (2019).

[15] A. A. Martin, N. P. Calta, S. A. Khairallah, J. Wang, P. J. Depond, A. Y. Fong, V. Thampy, G. M. Guss, A. M. Kiss, K. H. Stone, C. J. Tassone, J. Nelson Weker, M. F. Toney, T. van Buuren, and M. J. Matthews, Dynamics of pore formation during laser powder bed fusion additive manufacturing, Nat. Commun. **10**, 1987 (2019).

[16] T. R. Allen, W. Huang, J. R. Tanner, W. Tan, J. M. Fraser, and B. J. Simonds, Energy-Coupling Mechanisms Revealed through Simultaneous Keyhole Depth and Absorptance Measurements during Laser-Metal Processing, Phys. Rev. Appl. **13**, 064070 (2020).

[17] C. Körner, A. Bauereiß, and E. Attar, Fundamental consolidation mechanisms during selective beam melting of powders, Modell. Simul. Mater. Sci. Eng. **21**, 085011 (2013).

[18] A. Klassen, T. Scharowsky, and C. Körner, Evaporation model for beam based additive manufacturing using free

surface lattice Boltzmann methods, J. Phys. D: Appl. Phys. **47**, 275303 (2014).
[19] S. A. Khairallah, A. T. Anderson, A. Rubenchik, and W. E. King, Laser powder-bed fusion additive manufacturing: Physics of complex melt flow and formation mechanisms of pores, spatter, and denudation zones, Acta Mater. **108**, 36 (2016).
[20] W. King, A. T. Anderson, R. M. Ferencz, N. E. Hodge, C. Kamath, and S. A. Khairallah, Overview of modelling and simulation of metal powder bed fusion process at Lawrence Livermore National Laboratory, Mater. Sci. Technol. **31**, 957 (2015).
[21] W. Yan, W. Ge, Y. Qian, S. Lin, B. Zhou, W. K. Liu, F. Lin, and G. J. Wagner, Multi-physics modeling of single/multiple-track defect mechanisms in electron beam selective melting, Acta Mater. **134**, 324 (2017).
[22] H. Hertz, Ueber die Verdunstung der Flüssigkeiten, insbesondere des Quecksilbers, im luftleeren Raume, Ann. Phys. **253**, 177 (1882).
[23] R. W. Schrage, *A Theoretical Study of Interphase Mass Transfer* (Columbia University Press, New York, 1953).
[24] M. Knudsen, Die maximale Verdampfungsgeschwindigkeit des Quecksilbers, Ann. Phys. **352**, 697 (1915).
[25] R. Risch, Über die Kondensation von Quecksilber on einer vertikale Wand, Helv. Phys. Acta **6**, 127 (1933).
[26] C. J. Knight, Theoretical modeling of rapid surface vaporization with back pressure, AIAA J. **17**, 519 (1979).
[27] S. Anisimov, in *30 Years Of The Landau Institute–Selected Papers* (World Scientific, Singapore, 1996), Vol. 11, p. 14.
[28] T. Ytrehus, Molecular-flow effects in evaporation and condensation at interfaces, Multiphase Sci. Technol. **9**, 205 (1997).
[29] W. Tan and Y. C. Shin, Analysis of multi-phase interaction and its effects on keyhole dynamics with a multi-physics numerical model, J. Phys. D: Appl. Phys. **47**, 345501 (2014).
[30] C. Panwisawas, B. Perumal, R. M. Ward, N. Turner, R. P. Turner, J. W. Brooks, and H. C. Basoalto, Keyhole formation and thermal fluid flow-induced porosity during laser fusion welding in titanium alloys: Experimental and modelling, Acta Mater. **126**, 251 (2017).
[31] N. Kouraytem, X. Li, R. Cunningham, C. Zhao, N. Parab, T. Sun, A. D. Rollett, A. D. Spear, and W. Tan, Effect of Laser-Matter Interaction on Molten Pool Flow and Keyhole Dynamics, Phys. Rev. Appl. **11**, 064054 (2019).
[32] M. Bayat, A. Thanki, S. Mohanty, A. Witvrouw, S. Yang, J. Thorborg, N. S. Tiedje, and J. H. Hattel, Keyhole-induced porosities in laser-based powder bed fusion (L-PBF) of Ti6Al4V: High-fidelity modelling and experimental validation, Addit. Manuf. **30**, 100835 (2019).
[33] C. W. Hirt and B. D. Nichols, Volume of fluid (VOF) method for the dynamics of free boundaries, J. Comput. Phys. **39**, 201 (1981).
[34] J. Ahn and S.-J. Na, Three-dimensional thermal simulation of nanosecond laser ablation for semitransparent material, Appl. Surf. Sci. **283**, 115 (2013).
[35] Y. B. Zudin, *Non-Equilibrium Evaporation and Condensation Processes* (Springer, Switzerland, 2019).
[36] C. Cercignani, in *The Boltzmann Equation and Its Applications*, Applied Mathematical Sciences, edited by C. Cercignani (Springer, New York, NY, 1988).
[37] J. Ready, Effects due to absorption of laser radiation, J. Appl. Phys. **36**, 462 (1965).
[38] M. Arthur and C. Cercignani, Non-existence of a steady rarefied supersonic flow in a half-space, Z. Angew. Math. Phys. ZAMP **31**, 634 (1980).
[39] Y. Sone, S. Takata, and F. Golse, Notes on the boundary conditions for fluid-dynamic equations on the interface of a gas and its condensed phase, Phys. Fluids **13**, 324 (2001).
[40] R. Bellantone and Y. Hahn, Gas dynamics resulting from laser vaporization of metals in one dimension. I, J. Appl. Phys. **76**, 1436 (1994).
[41] A. Masmoudi, R. Bolot, and C. Coddet, Investigation of the laser–powder–atmosphere interaction zone during the selective laser melting process, J. Mater. Process. Technol. **225**, 122 (2015).
[42] H.-S. Tsien, Superaerodynamics, mechanics of rarefied gases, J. Aeronaut. Sci. **13**, 653 (1946).
[43] S. Ly, A. M. Rubenchik, S. A. Khairallah, G. Guss, and M. J. Matthews, Metal vapor micro-jet controls material redistribution in laser powder bed fusion additive manufacturing, Sci. Rep. **7**, 4085 (2017).
[44] P. B. Johnson and R. W. Christy, Optical constants of the noble metals, Phys. Rev. B **6**, 4370 (1972).
[45] H. Chen and W. Yan, Spattering and denudation in laser powder bed fusion process: Multiphase flow modelling, Acta Mater. **196**, 154 (2020).
[46] T. D. McLouth, G. E. Bean, D. B. Witkin, S. D. Sitzman, P. M. Adams, D. N. Patel, W. Park, J.-M. Yang, and R. J. Zaldivar, The effect of laser focus shift on microstructural variation of Inconel 718 produced by selective laser melting, Mater. Des. **149**, 205 (2018).
[47] J. Zhou, H. Li, Y. Yu, Y. Li, Y. Qian, K. Firouzian, and F. Lin, Research on aluminum component change and phase transformation of TiAl-based alloy in electron beam selective melting process under multiple scan, Intermetallics **113**, 106575 (2019).
[48] H. P. Tang, G. Y. Yang, W. P. Jia, W. W. He, S. L. Lu, and M. Qian, Additive manufacturing of a high niobium-containing titanium aluminide alloy by selective electron beam melting, Mater. Sci. Eng., A **636**, 103 (2015).
[49] W. Tan, N. S. Bailey, and Y. C. Shin, Investigation of keyhole plume and molten pool based on a three-dimensional dynamic model with sharp interface formulation, J. Phys. D: Appl. Phys. **46**, 055501 (2013).
[50] C. Zhao, Q. Guo, X. Li, N. Parab, K. Fezzaa, W. Tan, L. Chen, and T. Sun, Bulk-Explosion-Induced Metal Spattering During Laser Processing, Phys. Rev. X **9**, 021052 (2019).
[51] B. Zhou, J. Zhou, H. Li, and F. Lin, A study of the microstructures and mechanical properties of Ti6Al4V fabricated by SLM under vacuum, Mater. Sci. Eng., A **724**, 1 (2018).
[52] B. Zhang, H. Liao, and C. Coddet, Selective laser melting commercially pure Ti under vacuum, Vacuum **95**, 25 (2013).
[53] Y. Sato, M. Tsukamoto, and Y. Yamashita, Surface morphology of Ti-6Al-4V plate fabricated by vacuum selective laser melting, Appl. Phys. B **119**, 545 (2015).

[54] H. Chen, Y. Chen, Y. Liu, Q. Wei, Y. Shi, and W. Yan, Packing quality of powder layer during counter-rolling-type powder spreading process in additive manufacturing, Int. J. Mach. Tools Manuf. **153**, 103553 (2020).

[55] S. M. H. Hojjatzadeh, N. D. Parab, W. Yan, Q. Guo, L. Xiong, C. Zhao, M. Qu, L. I. Escano, X. Xiao, K. Fezzaa, W. Everhart, T. Sun, and L. Chen, Pore elimination mechanisms during 3D printing of metals, Nat. Commun. **10**, 3088 (2019).